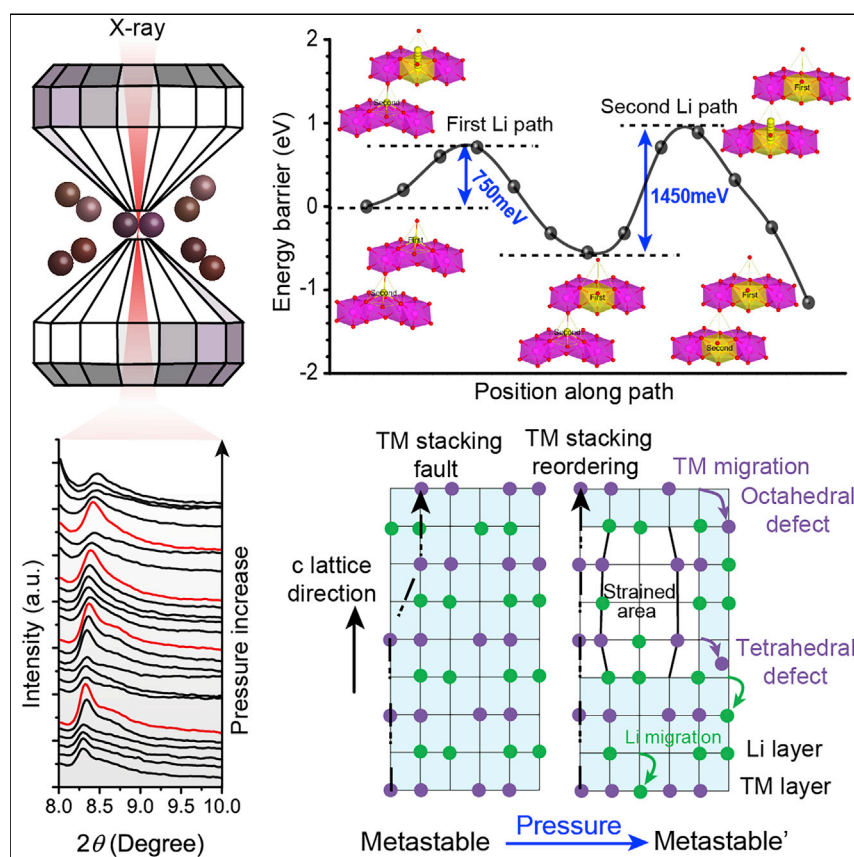## Article

High Pressure Effect on Structural and Electrochemical Properties of Anionic Redox-Based Lithium Transition Metal Oxides

Structural evolution plays a critical role in determining the intercalation reversibility of lithium, thereby influencing its electrochemical properties. This work reveals that structural flexibility and metastability are the characteristics of anionic redox-based lithium transition metal oxides. After anionic redox activation, these materials transform to metastable states that exhibit highly attractive mechanical properties (negative compressibility) and structural reordering under high pressure treatment.

Minghao Zhang, Bao Qiu, Jose M. Gallardo-Amores, ..., M. Elena Arroyo-de Dompablo, Zhaoping Liu, Ying Shirley Meng

liuzp@nimte.ac.cn (Z.L.)
shmeng@ucsd.edu (Y.S.M.)

HIGHLIGHTS

Structural flexibility and metastability of anionic redox-based materials

Structure reordering and strain accumulation under high pressure

Negative bulk compressibility induced by the defect formation

3 **Understanding**
Dependency and conditional studies on material behavior

Matter

CellPress
OPEN ACCESS

Article

High Pressure Effect on Structural and Electrochemical Properties of Anionic Redox-Based Lithium Transition Metal Oxides

Minghao Zhang,[1,5] Bao Qiu,[2,5] Jose M. Gallardo-Amores,[3] Marco Olguin,[1] Haodong Liu,[1] Yixuan Li,[1] Chong Yin,[2] Sheng Jiang,[4] Weiliang Yao,[1] M. Elena Arroyo-de Dompablo,[3] Zhaoping Liu,[2,*] and Ying Shirley Meng[1,6,*]

SUMMARY

The richness of anionic redox chemistry in the solid state offers new opportunities and a possible paradigm shift in energy storage. The excess capacity that goes beyond conventional theoretical values is attributed to the anionic redox in Li-rich transition metal oxide cathodes for Li-ion batteries. Their electrochemical behavior is thermodynamically determined by structural evolution. To better understand the electrochemical dependence on structural factors, we have induced structural modifications in pristine and electrochemically activated $Li_{1.144}Ni_{0.136}Co_{0.136}Mn_{0.544}O_2$ through high-pressure treatment. A unique cyclical change of structural reordering is observed in the anionic redox-activated material during operando pressure sweep, characterized by a periodic evolution of superlattice peak intensity in synchrotron X-ray diffraction patterns. During the structural reordering period, the bulk compressibility of the material decreases, even becoming negative. These insights elucidate the structural flexibility and metastability of anionic redox-based materials, which can undergo large compressions and structural modifications while delivering good electrochemical properties.

INTRODUCTION

In classical cathode intercalation compounds for Li-ion batteries, such as $LiCoO_2$ and $Li(Ni_{1-x-y}Mn_xCo_y)O_2$, the electric charge is stored by reversible Li intercalation coupled to transition metal (TM) cation redox.[1] The charge storage capacity is thus restricted by Li stoichiometry and the formal oxidation state of the TM in classical compounds. There has been increasing interest in introducing an over-stoichiometry of Li to surpass the conventional mechanism of formal TM redox (Figure S1).[2,3] Several reports have demonstrated that anion (oxygen) redox in these materials is the main reason for the high reversible capacity at room temperature.[4–7] We propose that an additional unhybridized O 2p orbital, derived from the excess Li in the TM layer, causes oxygen oxidation, which contributes to the extra capacity.[8] After oxygen redox activation, either localized electron holes or oxygen dimers tend to form in the bulk structure while oxygen gas evolution occurs at the particle surface, leaving oxygen vacancies and an under-coordinated TM.[9] The exact mechanism at the molecular/atomic scales remains largely under debate.

It is well documented that the structural evolution plays a critical role in determining the reversibility of oxygen redox, thereby influencing the electrochemical properties. Work

Progress and Potential

Transition metal oxide is one of the most interesting classes of solids, exhibiting many physical properties, including magnetism, piezoelectricity, and superconductivity. Lithium transition metal oxide is the cornerstone for energy storage through Li intercalation. This work demonstrates that the formation of structural defects during the electrochemical activation process results in metastable states in lithium transition metal oxides. The unique metastability provides an opportunity to reveal the unusual properties of complex oxide materials, such as negative thermal expansion and negative bulk compressibility. Predictive design for new materials with extraordinary combinations of physical characteristics can be realized by electrochemically controlling the lithium intercalation process.

Matter
Article

by Gent et al. [10] ascribed drastic change in the local oxygen coordination environments associated with the migration of the TM interlayer to the cycling voltage hysteresis. Sequence changes of oxygen stacking induced by the dislocation network were also observed in nanoparticles of lithium-rich layered oxide material, which contributes to the voltage decay in long-term cycling.[11] Hu et al.[12] observed large pores in the interior of the electrochemically cycled particle due to oxygen release within particles, leading to attenuation of energy during battery cycling.[12] Our recent work has demonstrated various structural defects, including lithium vacancies in the TM layer, stacking faults in the TM layer, and local distortion of the oxygen framework, resulting in the unique metastable state, which is responsible for the voltage hysteresis and decay.[13] Assat et al.[14] investigated the thermal effects of voltage hysteresis in anionic redox-based cathodes and found that metastable electrochemical paths persist even under quasi-static conditions.

The cycled state is a metastable state because of the relatively higher energy and the large energy barrier that the system cannot overcome to relax toward the stable state through electrochemical processes at room temperature. In our previous work, the thermal effect on cation and anion redox-based cathode material was directly compared with show that the metastable state is the key feature of Li-rich layered nanoparticles.[13] Thermal energy can effectively eliminate defects in the cycled structure so that the structure and voltage can both be recovered. More intriguingly, we reported negative thermal expansion of the cycled Li-rich layered materials within a specific temperature range while preserving the original layered phase. It is proposed that materials that contract on heating, in general, can also expand under hydrostatic pressure.[15] This rule inspires one to ponder whether mechanical energy (high pressure treatment in the scale of GPa) can potentially serve as a driving force, similar to thermal energy, to recover the cycled state.

It has been reported previously that high pressure treatment of electrode materials is a powerful tool to induce structural modifications that are not typically possible at atmospheric pressure and which result in different electrochemical characteristics.[16–18] For compressible cathode materials, the high pressure treatment combined with high temperature may induce severe structural phase transformations (for instance, olivine-spinel $LiCoPO_4$).[19] Layered cathode materials are materials that are not very compressible (bulk modulus in the range of 120–150 GPa), yet important structural modifications have been reported. Zhang et al.[20] studied the high pressure behavior of pristine Li-rich layered oxide $Li[Li_{0.1}Ni_{0.35}Mn_{0.55}]O_2$ up to 19.7 GPa. The material remained in the layered phase and an obvious structure compression was observed. The electrochemistry of the pressure-treated materials was not explored. Fell et al.[21] compared structural modifications in $LiNi_{0.5}Mn_{0.5}O_2$ and $Li[Ni_xLi_{1/3-2x/3}Mn_{2/3-x/3}]O_2$ (this is an Li-excess material with x = 1/4 and 1/2) using high pressure–high temperature treatment. After the treatment, the Li-excess materials displayed superior electrode characteristics to $LiNi_{0.5}Mn_{0.5}O_2$ whose electrochemical characteristics deteriorated due to the structural modifications. Despite the above high pressure research on layered cathode materials, little is known about the effect of high pressure on their electrochemically cycled structure.

The aim of this research is to investigate high pressure effects on the electrochemically cycled structure of anionic redox-based oxides. For this, a pristine and a cycled Li-excess material ($Li[Li_{0.144}Ni_{0.136}Co_{0.136}Mn_{0.544}]O_2$, denoted as LR-NCM) were subjected to static pressure treatments in two types of high pressure cells: diamond anvil cells (DACs) up to 15 GPa and large anvil cells (LACs) in a Belt-type press up to 4 GPa. The combination of the two approaches in junction with molecular dynamics (MD) simulations reveal the occurrence of structural reordering upon pressure,

[1]Department of NanoEngineering, University of California San Diego (UCSD), La Jolla, CA 92093, USA

[2]Ningbo Institute of Materials Technology and Engineering (NIMTE), Chinese Academy of Sciences, Ningbo 315201, P. R. China

[3]Departamento de Química Inorgánica, Facultad de Ciencias Químicas, Universidad Complutense de Madrid, 28040 Madrid, Spain

[4]Shanghai Advanced Research Institute, Chinese Academy of Sciences, Shanghai 201210, P. R. China

[5]These authors contributed equally

[6]Lead Contact

*Correspondence: liuzp@nimte.ac.cn (Z.L.), shmeng@ucsd.edu (Y.S.M.)

https://doi.org/10.1016/j.matt.2020.10.026
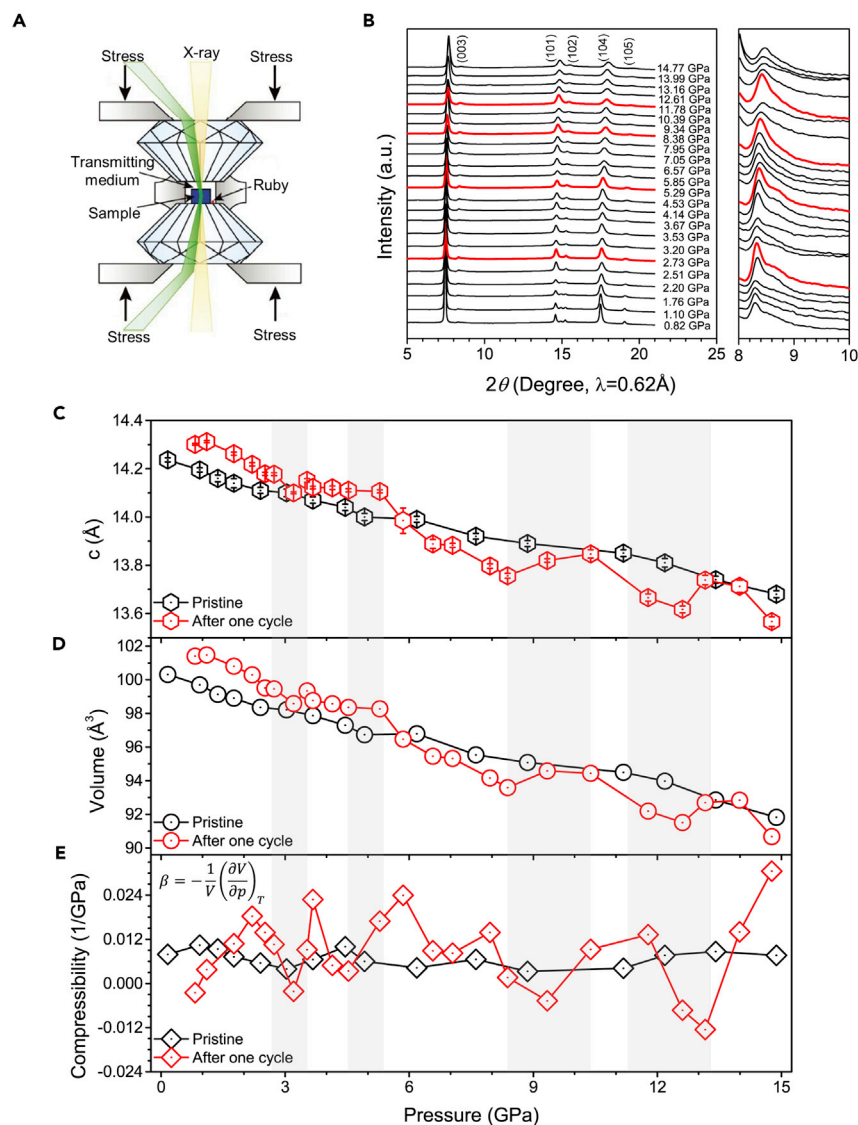
Matter
Article

CellPress
OPEN ACCESS

although with incrementally increasing antisite defects and microstrain. We show that all of these structural modifications have a profound impact on the electrochemical properties of the material after high pressure treatment. Larger Li (de)intercalation capacity is obtained for the pressure-treated sample, yet with lower average discharge voltage. These results demonstrate the flexibility and metastability of the cycled anionic redox-based cathode material, in which crystal defects are of great importance.

RESULTS

Reordering of Cycled Li-Rich Layered Oxide Induced by High Pressure

The same batch of cycled LR-NCM, as applied in our previous work,[13] was loaded into a DAC for a high pressure sweep. Figure 1A illustrates the DAC working mechanism, in which a transmitting medium allows isotropic pressure to be applied to the sample. Operando synchrotron X-ray diffraction (SXRD) data were then collected to reveal the structural evolution during the pressure treatment. As shown in Figure 1B, the cycled structure remains phase pure with an R-3m space group up to ~15 GPa at room temperature. Obvious peak broadening is observed in the SXRD patterns with the increase of applied pressure, which is a strong indication of continuous formation of microstrain in the bulk structure. The peak at ~2θ = 8.4° highlighted in the enlarged region of Figure 1B is attributed to Li and TM honeycomb superstructure ordering within the TM layers.[22] It is well documented that the superstructure gradually disappears, and that the material becomes partially disordered during the initial electrochemical cycle.[11] One remarkable change in the SXRD patterns is that the superlattice peak intensity becomes intensified and weakened in a periodic pattern during the high pressure processing. The peak intensity reaches its maxima at pressure values of 2.73, 5.29, 8.38, and 11.78 GPa. The evolution of the superlattice peak indicates that the structure ordering can be recovered under certain pressure conditions.

A high pressure sweep in the same range was also conducted on the pristine LR-NCM electrode and the SXRD patterns recorded are shown in Figure S2. The results show that all diffraction peaks shift to larger angles with increasing pressure and that the superlattice peaks in the 2θ range of 8°–9° are retained. These results for the pristine electrode are consistent with previous work by Zhang et al.[20] and follow the normal pressure effect on inorganic ceramic materials. Rietveld refinements of the patterns for the pristine material demonstrate that the material is maintained in a layered structure. The pressure dependence of lattice parameters of pristine and initially cycled LR-NCM is presented in Figure 1C. For the pristine sample, the c lattice parameter almost linearly decreases by ~4% from 14.237(8) to 13.680(1) Å as the pressure increases. After electrochemical cycling, the unit cell volume is known to expand, with lattice parameters increasing.[23] The c lattice parameter for the cycled sample reduces more than 5% in the full range of the pressure sweep. The larger reduction found for the initially cycled LR-NCM suggests that the electrochemical reaction produces a softer and more compressible material. Unlike the linear decrease for the pristine sample, the c lattice parameter of the cycled sample shows an obvious expansion period as the superstructure ordering is recovered (see the shaded area in Figure 1C). The sharp contrast between the pristine and cycled samples is also observed in the change of the a lattice parameter as the pressure increases (Figure S3). Note that the reduction percentage of the a lattice parameter is smaller than that of the c lattice parameter for both the pristine (2.3%) and cycled samples (2.9%). The lattice is more susceptible to deform along the c axis under pressure and this is correlated to the different compressions of the inter-plane and in-plane bonds between adjacent metal ions.[21]

Figure 1. Reordering and Negative Compression of Cycled Li-rich Layered Oxide under High Pressure Treatment

(A) Schematic image of symmetric DAC for operando SXRD measurement under different pressures.

(B) Normalized SXRD pattern of the LR-NCM electrode after initial cycle under different pressure using DAC.

(C and D) lattice parameter and unit cell volume evolution obtained from SXRD refinement under different pressure using DAC. Error bars indicate one standard deviation.

(E) Calculated compressibility under different pressure of the pristine and initially cycled LR-NCM based on refined unit cell parameters.

The effect of pressure on unit cell volume for the pristine and initially cycled samples is calculated in Figure 1D. The anomalous expansion behavior of the cycled sample under increasing pressure results from the evolution of the lattice parameters. The $P–V$ data up to 15 GPa are fitted to the third-order Birch-Murnaghan equation of the state.[24] The pristine and cycled LR-NCM exhibits bulk moduli of 117 and 111 GPa, respectively. These values are lower than the bulk modulus found for classical layered oxide $LiCoO_2$ (149 GPa) and $LiNi_{0.5}Mn_{0.5}O_2$ (125 GPa).[21] The LR-NCM

Matter
Article

material is more compressible than the stoichiometric layered oxide due to the presence of Li ions in the TM layer. The material compressibility, reciprocal of the bulk modulus, is calculated based on the expression in Figure 1E. The absolute compressibility value of the cycled sample is much larger than that of the pristine sample. The compressibility of the pristine sample is positive for all the testing pressure and does not vary obviously as pressure increases, whereas the cycled material displays a negative bulk compressibility in the pressure range as anomalous unit cell volume expansion takes place. This negative compressibility effect once again manifests in the unique cycled structure response to the applied pressure. Similar to the thermal effect, as reported previously,[13] the cycled LR-NCM structure is induced to oppose the volume change as the external force increases. The sinusoidal waveform of the evolution of compressibility implies that the structure reordering is sensitive and recurrent to the applied mechanical force.

Lithium Migration and Reordering of the TM Stacking Sequence

It has been reported that, during electrochemical cycling, lithium from the TM layer is largely irreversible with formation of vacancies, which could induce TM ions in-plane migration.[23] The in-plane TM migration does not alter the global layered structure, while largely disturbing the honeycomb superstructure within the TM layers. It is also demonstrated that TM in-plane reordering accompanies lithium reinsertion in the TM layer due to the energy penalty.[13] To investigate the superstructure reordering process induced by high pressure, the cycled LR-NCM sample was exposed to different hydrostatic pressure using a Belt-type press in the range of 1.0–4.0 GPa for 0.5 or 1.5 h at room temperature. The pressure was then slowly released, and the obtained powder was collected under argon atmosphere for further testing at ambient pressure. The use of the LAC in the Belt apparatus allows the preparation of sufficient samples (~0.5 g) for multiple characterization tasks with a better signal-to-noise ratio. The high pressure range (1–4 GPa) where the first superstructure reordering occurs was selected based on operando pressure sweep analysis.

The *ex situ* SXRD data for the pristine sample are shown in Figure S4. The detail refinement results using both the R-$3m$ and $C2/m$ symmetry were summarized in Table S1. Note that the major difference between the two structure models is the ideal Li/TM ordering assumption in the $C2/m$ symmetry. The results show that atomic occupancy is independent of selected symmetry between R-$3m$ and $C2/m$. Compared with that using R-$3m$ symmetry, a worse R factor is obtained for the $C2/m$ symmetry due to the ideal ordering assumption. After cycling, the Li/TM ordering in the TM layer is mostly lost, which makes R-$3m$ symmetry more appropriate for structural refinement. Figure S5 shows the refined *ex situ* SXRD patterns using R-$3m$ symmetry for pristine and initially cycled samples treated with different Belt-type pressures for 0.5 or 1.5 h. After electrochemical cycling, the lattice parameters a and c increase to 2.8582(3) and 14.320(4) Å, respectively (Table S2). All the Belt-type pressure-treated samples display pure layered phases, and the a lattice parameter is observed to increase after pressure treatment, except for the sample that underwent a pressure of 4.0 GPa for 1.5 h. This lattice expansion phenomenon is consistent with the observations from the operando pressure sweep. For the atomic occupancy refinement, the pristine sample composition is determined by inductively coupled plasma measurement and the composition of the cycled sample is inferred from the electrochemical testing results. Oxygen vacancies were identified in the cycled sample and showed no obvious change after the pressure treatment. The migration barrier can be as high as 2 eV, which makes oxygen vacancy migration nearly impossible even under high pressure.[25] Oxygen vacancies result in a large fraction of under-coordinated cations, which can potentially migrate to fully coordinated octahedral

⬡ CellPress
OPEN ACCESS

Matter
Article
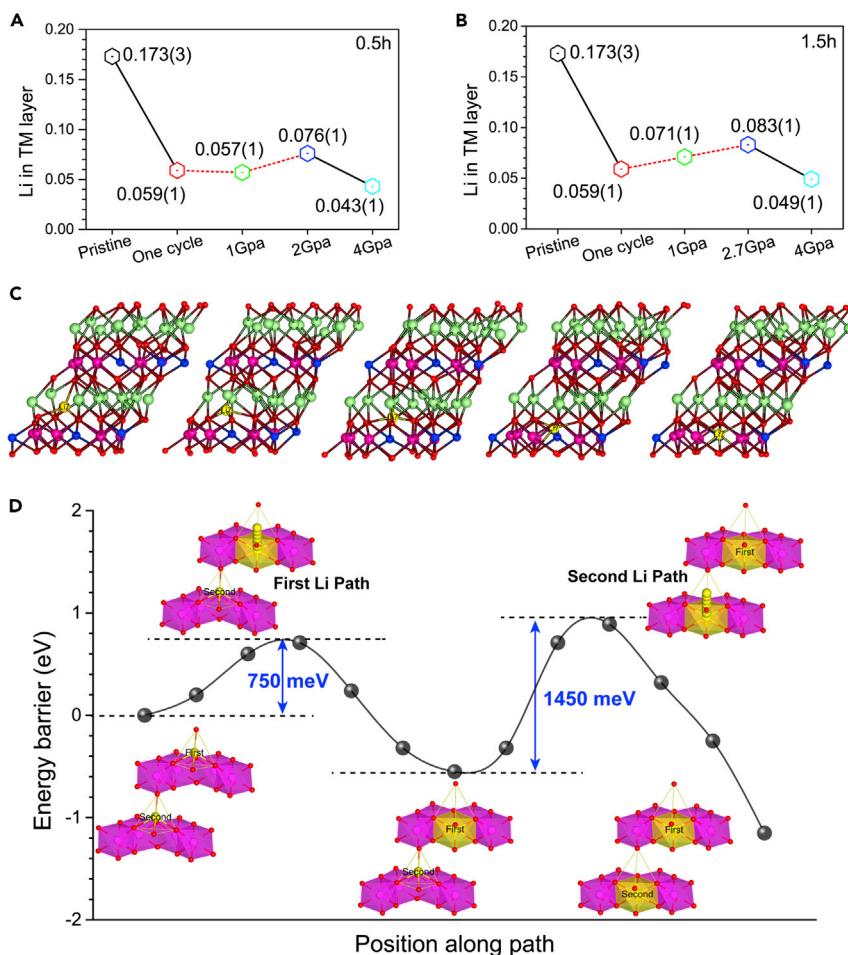
Figure 2. Lithium Migration Pathway and Energy Barrier for Structural Reordering Induced by High Pressure Treatment

(A and B) Changes of the occupancy of Li ions in the TM layer obtained from *ex situ* SXRD refinement for pristine and initially cycled LR-NCM samples treated with different Belt-type pressures for 0.5 or 1.5 h.

(C) Snapshots from the MD simulations showing the spontaneous relaxation of Li from the Li layer to the TM layer in the cycled Li-rich layered structure applied at a pressure of 2 GPa (green, Li; purple, Mn; blue, Ni; red; oxygen; yellow, migrated Li).

(D) Calculated path and energy barrier for Li migration identified in MD simulations from the Li layer to the TM layer using the NEB method.

sites nearby due to different driving forces.[26] Rietveld analysis indicates that, after the initial cycle, the lithium occupancy in the TM layer decreases to 0.059(1) from 0.173(3) of the pristine sample (Figure 2A), while the sample treated with 2 GPa for 0.5 h has ~30% more lithium in the TM layer compared with the cycled sample. The lithium migration into the TM layer is not observed for the sample with further increase of Belt-type pressure to 4 GPa. The trend in lithium migration is confirmed by the other set of samples pressure treated for 1.5 h, where the maximum lithium occupancy in the TM layer reaches 0.083(1) for the sample treated with 2.7 GPa (Figure 2B). The elimination of lithium vacancies in the TM layer recovers local Li-excess environments around oxygen, which is crucial for oxygen redox activity.[4] In addition, occupancy of TM ions in the lithium layer (antisite defects Ni_{Li}) starts to increase for the sample treated with a pressure greater than 2 GPa (Table S2), which could hinder lithium diffusion through the layer.

Matter
Article

CellPress
OPEN ACCESS

The effect of pressure on lithium migration was then modeled by MD solid-state simulation using density functional theory (DFT). Isotropic pressure and room temperature, close to experimental conditions, were applied to isolate the mechanical effect from the thermal effect on lithium migration. The simulations were performed on a supercell model composed of two-formula units of $Li_{14}Ni_3Mn_7O_{24}$. In this model, there are two "excess" Li ions located in the TM layer. A specific $Li_{11/14}$ concentration with one oxygen vacancy was chosen to simulate the discharged state ($Li_{11}Ni_3Mn_7O_{23}$), in which both Li ions are absent in the TM layer. The external pressure applied and the temperature as a function of the simulation time are shown in Figure S6. The external pressure and temperature were stabilized after 20 ps. Lithium migration to the TM layer began to take place at ~22 ps in the structure that underwent a pressure of 2 GPa (Video S1), while no lithium migration was observed for the MD simulation with 4 GPa (Video S2), which is consistent with the *ex situ* SXRD refined results. The energetically most favorable route for lithium migration proceeds through the oxygen layer, as shown in Figure 2C, with the migrated Li-ion highlighted in yellow. Note that TM migration from the TM layer to the Li layer was not captured in the MD simulation due to the higher activation barrier (1 eV for Ni^{2+} and 2.6 eV for Mn^{4+}) compared with Li.[26] Thus, it will take a much longer simulation time to capture TM migration, in particular under room temperature conditions.

The nudged elastic band (NEB) method was then applied to determine the minimum energy paths for Li migration, with the initial and final structure identified in MD simulations. Firstly, the total energy for the supercell decreases by ~0.5 eV when locating one Li (equivalent to moving 4.5% Li back) in the TM layer (Figure 2D). After relaxation, the supercell volume of the final state expands to 841.6 $Å^3$ from 840.5 $Å^3$ of the initial state. The minimum energy path for Li migration proceeds from the tetrahedral site in the lithium layer to the empty octahedral site in the TM layer through the shared oxygen plane. The activation barrier for this path is approximately 0.75 eV, as shown in Figure 2D. We further investigated the migration of the second Li that had the same crystallographic symmetry as the first Li in the supercell. Although the migration path is almost the same as the first Li, the activation barrier for the second Li increases to 1.45 eV. After the migration of the second Li, the supercell volume further expands to 842.1 $Å^3$ with a total energy reduction of ~0.5 eV. Based on the energy evolution along the migration path, the recurring unit cell volume expansion and superstructure ordering during the operando pressure sweep can be explained as follows: (1) the high energy barrier (0.75 eV) makes lithium migration nearly impossible under ambient conditions, and sufficient driving force (e.g., 2 GPa) is required to activate the process; (2) once lithium migration to the TM layer is activated, the materials relax to the stable state from the metastable state, with energy reduction through expansion opposing the external pressure effect; (3) further increase of the external pressure (e.g., 4 GPa) will trigger the reversed migration for the same Li since the energy barrier for the backward process is only 0.5 eV higher than the forward process; (4) at equilibrium pressure, the net Li migration rate will be zero, no structural reordering will be observed, and the external pressure will increase the system energy by normal compression; (5) the next structural reordering cycle will occur when the applied pressure (e.g., 5.5 GPa) is adequate to overcome the larger barrier (1.45 eV) for the second lithium migration. In this regard, the lithium migration process induced by different pressures is fundamentally the same, with the exception of the activation energy. Higher pressure is predicted to result in larger lithium migration to the TM layer as well as other structural evolution, including TM migration.
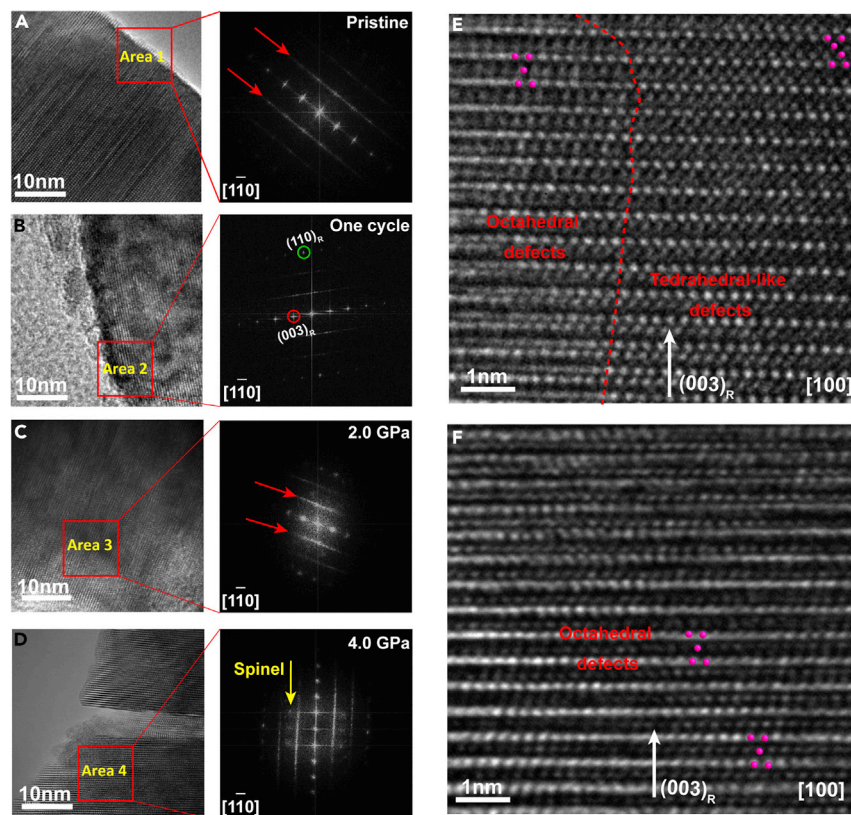
Figure 3. Stacking Sequence Reordering and Antisite Defects Formation under High Pressure Treatment

(A–D) TEM image and its corresponding FFT pattern for pristine (A) and initially cycled LR-NCM samples (B) treated with different Belt-type pressures for 1.5 h (C and D). The elongation of these spots are along the $[1–10]_R$ direction. The spots indicated by red arrows represent the (110), (020), and (−110) lattice planes of the monoclinic Li_2MnO_3 (denoted as M). The spot marked by the red circle is shared by the $(003)_R$ lattice plane of the rhombohedral (denoted as R) phase. The spot marked by the green circle is shared by the $(110)_R$ lattice plane of the rhombohedral phase.

(E) HRTEM image for the initially cycled sample after Belt-type pressure treatment at 2.7 GPa for 1.5 h.

(F) HRTEM image for the initially cycled sample after Belt-type pressure treatment at 4 GPa for 1.5 h. An atomic structure model is provided in (E) and (F) for the octahedral or tetrahedral defect regions, respectively.

The superlattice peak intensity in the SXRD patterns is not only dependent on the in-plane ordering, but also on the TM stacking sequence perpendicular to the planes.[27,28] To visualize the material structural change from the atomic level, transmission electron microscope (TEM) images of particles from different samples were obtained and are shown in Figures 3A–3D. The same zone axis [1–10] of R-$3m$ structure were determined for all the samples by matching the lattice spacing in TEM images with their fast Fourier transform (FFT) patterns. Two characteristic spots $(003)_R$ and $(110)_R$ are indicated in the patterns. The pristine sample (Figure 3A) shows a clearly resolved layered structure that extends to the surface of the particle and fairly intense diffraction streaks, indicated by red arrows, in the corresponding FFT pattern. The intensity of the diffraction streaks reflects TM ordering along the stacking direction of the layers.[29] Our previous results using SingleCrystal simulation demonstrated that over 30% TM stacking faults exist in the pristine particle.[13] After electrochemical cycling, the particles start to encounter a larger degree of defects,

Matter
Article

CellPress
OPEN ACCESS

including TM stacking faults that result in foggy atomic resolution imaging and weak diffraction streaks in the FFT pattern (Figure 3B). After pressure treatment, the intensity of the diffraction streaks becomes stronger and the bulk layered structure is again evident. The intensified diffraction streaks imply that the stacking faults generated in the bulk structure during electrochemical cycling can be partially eliminated by pressure treatment so that structural ordering along the stacking direction of the layers is partially restored.

Li/TM Antisite Defects and Bulk Strain Accumulation

Although the bulk structure maintains the layered phase after pressure treatment, the surface is transformed to a spinel-type structure, as highlighted by yellow arrows in Figure 3D. High-resolution TEM (HRTEM) images were recorded for the samples treated with different Belt-type pressures for 1.5 h (Figures 3E and 3F). Similar to the FFT observations, TM ions were found in the Li layer in the surface and subsurface regions, forming a defect spinel structure. It is worth noting that both tetrahedral and octahedral defects were found for the sample treated at 2.7 GPa. With a pressure increase to 4 GPa, the tetrahedral defects in the sample vanished (Figure 3F). We hypothesize that the TM in the tetrahedral position is a transition state after TM out-of-plane migration is activated. TM ions hopping between neighboring octahedra must occur via an intermediate tetrahedral site considering that these are the only empty sites available in the structure. The TM located in the tetrahedral positions thus represents local but not absolute minima in the energy landscape, which can be eliminated by a larger external driving force (i.e., higher pressure). This hypothesis is supported by recent work on phase transition in the $LiNiO_2$ cathode material, where nickel atoms in tetrahedral positions were observed in the phase transition region.[30] Figure S7 presents the crystal structure of the initially cycled Li-rich layered oxide before and after the pressure treatment based on SXRD refinement and HRTEM imaging. To clearly illustrate the reordering process, only point defects are considered for both bulk and surface regions. For the bulk region, the elimination of lithium vacancies in the TM layer with pressure treatment recovers local Li-excess environments. For the surface region, occupancy of TM ions starts to increase in the lithium layer.

The changes of the surface structure and the oxidation state of TM were also monitored by scanning transmission electron microscopy/electron energy loss spectroscopy (STEM/EELS). Figures 4A–4F compare the EELS spectra of the O K and TM L-edges from the surface and subsurface region of the crystal as indicated in annular dark field (ADF) STEM images for different samples. The O K-edge EELS corresponds to the transition from O 1s states to unoccupied O 2p states in the conduction band. Due to the TM 3d-O 2p hybridization, O K-edge spectra also reflect the covalency of TM-O bonding.[31] A clear pre-peak in the O K-edge is obtained from both the subsurface and surface region of the pristine particle. This pre-peak starts to decrease when it arrives at the surface region of the sample after electrochemical cycling. The decrease of the pre-peak can be ascribed to the oxygen vacancy formation and reduction of TM-O bond covalency. After 4 GPa pressure treatment, the pre-peak completely disappears in the near surface due to the formation of the defect spinel structure as identified by HRTEM imaging. The TM reduction usually appears with defect spinel structure formation due to charge compensation.[32] This is verified by the L_3/L_2 peak intensity ratio in the Mn L-edge (Figure 4F). The Mn L_3- and L_2-edges are a result of the transition from $2p_{3/2}$ and from $2p_{1/2}$ to 3d states, respectively. Previous studies have shown that the L_3/L_2 ratio is inversely proportional to the oxidation state of Mn.[33] The most salient change of the Mn L-edge spectra is the increase of the L_3/L_2 ratio in the near surface for the sample that

CellPress
OPEN ACCESS

Matter
Article
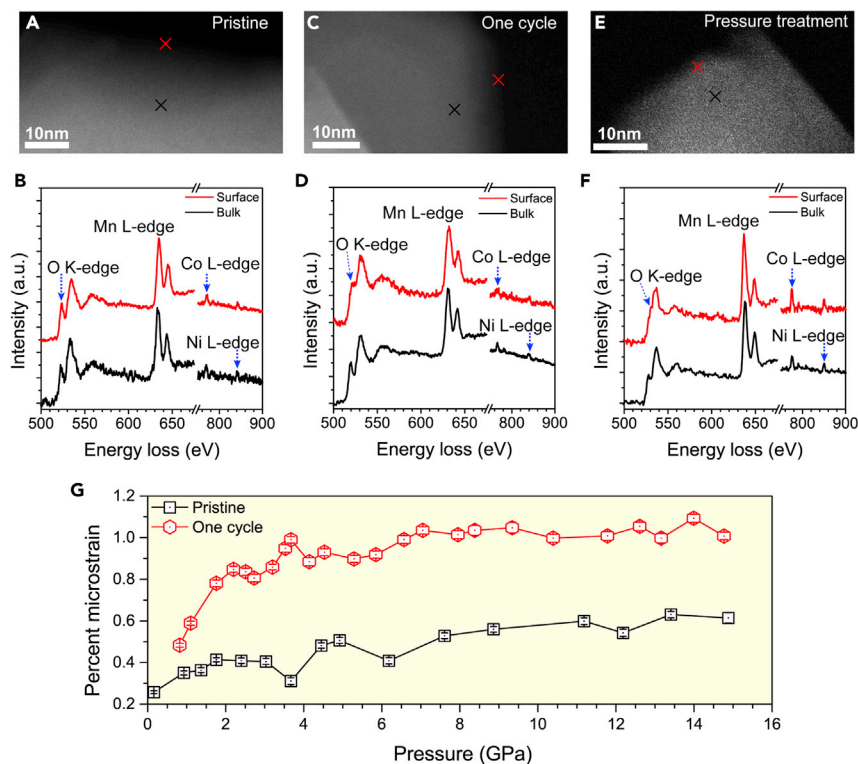
Figure 4. Composition Redistribution and Bulk Strain Accumulation after High Pressure Treatment

(A and B) STEM image and EELS spectra for pristine the LR-NCM sample.

(C and D) STEM image and EELS spectra for the initially cycled LR-NCM sample.

(E and F) STEM image and EELS spectra for the initially cycled sample after Belt-type pressure treatment at 4 GPa for 1.5 h.

(G) Changes of percent microstrain, obtained using SXRD, for a pristine LR-NCM electrode and for the electrode after an initial cycle under different pressures using DAC. Error bars indicate one standard deviation.

underwent pressure treatment at 4 GPa, which indicates a lower oxidation state of Mn in the surface defect region. In addition, the sharp increase of Co and Ni L-edge peak intensity in the surface region of the pressure-treated sample implies the occurrence of TM segregation during pressure treatment. The surface TM segregation is demonstrated to be facet dependent by STEM/energy dispersive spectroscopy (EDS) line scan as shown in Figure S8. The Co- and Ni-rich layer can be approximately 10 nm from the surface until close to the designed bulk TM stoichiometry.

The evolution of particle morphology and internal strain under high pressure can also fundamentally alter the physical property, structural stability, and electrochemical activity of the materials.[34] Figure S9 shows scanning electron microscope (SEM) images for the initially cycled samples treated in the Belt-type press for 1.5 h. The obtained cycled samples contain spherical LR-NCM particles of 10–20 μm and nano-sized conductive additive and binder. Interestingly, after pressure treatment, no significant changes of particle size distribution are observed based on the images analysis, which implies that serious cracks do not appear within the spherical particles. Indeed, with the increase in pressure, the particle internal strain builds up without release through mechanical fracture. The evolution of microstrain during the operando pressure sweep was extracted by examining the Bragg peak broadening

Matter
Article

CellPress
OPEN ACCESS

observed in the SXRD patterns using the Williamson-Hall method.[35] As shown in Figure 4G, the microstrain is observed to build up for both pristine and initially cycled samples with the increase of the operando pressure. More internal strain is stored in the cycled LR-NCM sample due to the increased disorder of the bulk structure. Microstrain analysis was also applied for the samples treated with different Belt-type pressure and the results are shown in Figure S10. After the Belt-type pressure was slowly released, a considerable amount of internal strain persists in the collected powder under ambient conditions. The amount of residue microstrain is proportional to the applied pressure, which follows the same trend observed in the operando DAC pressure sweep. The set of samples treated with different Belt-type pressures for 1.5 h were selected for the electrochemical performance testing.

DISCUSSION

High Pressure Effect on Electrochemical Properties

To assess the effect of high pressure on electrochemical properties, coin-type half cells were assembled using treated LR-NCM samples as the cathodes and Li metal as the anode. Figure S11 shows the first charge–discharge curves of the initially cycled samples treated with different Belt-type pressure in the voltage range of 2.0–4.8 versus Li^+/Li^0. The pressure-treated samples exhibit larger charging and discharging capacity than the untreated samples, which is due to Li-ion reinsertion into the TM layer confirmed by the SXRD refinement and MD simulation results. Consequently, the specific Li-O-Li configurations are recovered after pressure treatment, leading to the electrochemically active oxygen states.[36] This can well explain the initially cycled LR-NCM followed by pressure treatment at 2.7 GPa, with the maximum lithium occupancy in the TM layer showing the largest reversible capacity among the samples. However, compared with the initial cycle, the charging plateau region due to anionic redox activity at approximately 4.5 V disappears in all the samples, regardless of pressure treatment or not. The average discharge voltage decreases and shows a faster decay trend with subsequent cycles for the pressure-treated samples (Figure S12). It is apparent from Figure S13 that the sample showing a larger residue microstrain due to higher pressure treatment shows worse cycling stability.

With large structural modifications induced by high pressure, the cycled LR-NCM can still deliver reasonable electrochemical performance, which manifests the structural flexibility of Li-rich layered oxide. While the ductility is much lower for the TM cation redox-based classical layered oxide material, it can only yield one-third of original capacity after a high pressure treatment of the same magnitude.[21] The different structural flexibility between the two types of cathode materials can be mainly due to: (1) compositional difference, where most of the classical layered materials are Ni rich ($LiNi_{0.8}Co_{0.15}Al_{0.05}O_2$, $LiNi_{0.8}Co_{0.1}Mn_{0.1}O_2$, $LiNi_{0.6}Co_{0.2}Mn_{0.2}O_2$) and Li-excess materials are typically Mn rich ($Li_{1.2}Ni_{0.2}Mn_{0.6}O_2$, $Li1_{.144}Ni_{0.136}Co_{0.136}Mn_{0.544}O_2$). Generally, the TM–O bonding will be more rigid for cations with stronger covalency (e.g., Ni^{4+}) relative to those with stronger ionicity (e.g., Mn^{4+}).[7] (2) Defect density difference, where the number of dislocations formed in the classical layered material is significantly less than in Li-rich layered oxide after electrochemical cycling.[11] When a mechanical force is applied to the cycled material, the dislocations can potentially move through the lattice structure, which helps explain why Li-excess materials are so ductile.

When compared with the heat-treated sample in our previous work,[13] although the superstructure reordering effect is similar, the voltage recovery was not found for the pressure-treated samples. The heat-treated sample also shows better capacity
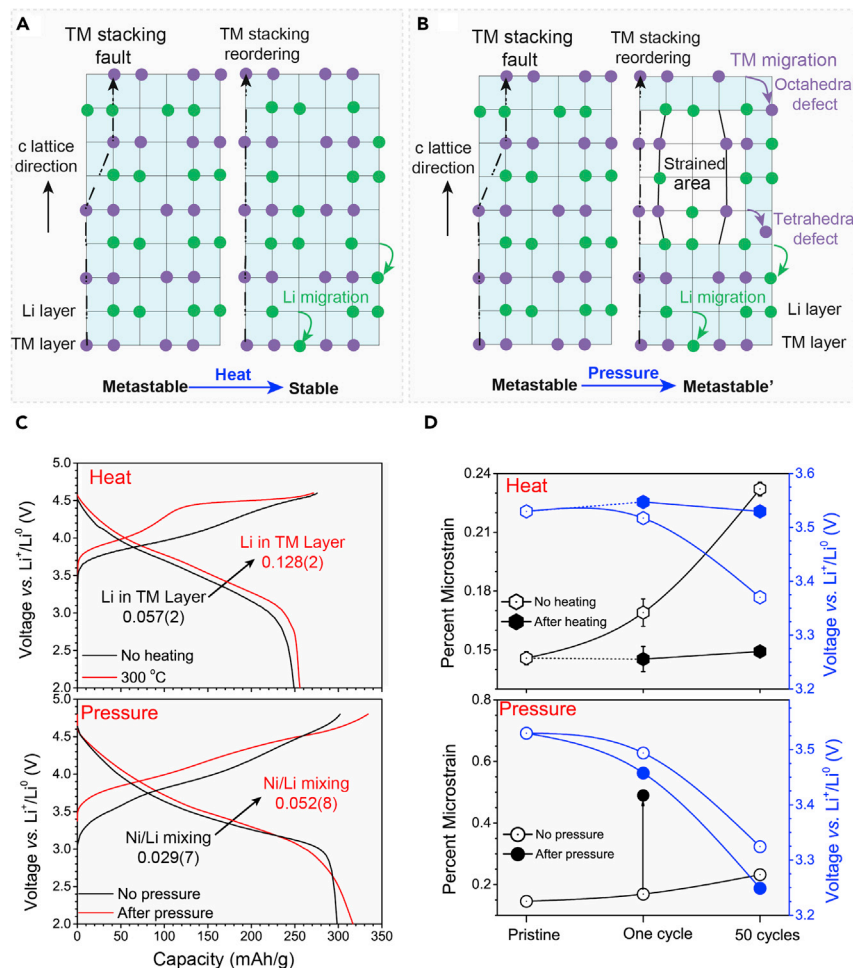
Figure 5. High Pressure Effect on Electrochemical Properties and Structural Defect States

(A and B) Schematic illustration of the structure evolution for cycled LR-NCM under heat or pressure treatment (green, Li; purple, TM).

(C) The first charge–discharge voltage curves of the initially cycled LR-NCM under heat or pressure treatment.

(D) Changes of percent microstrain and average voltage for LR-NCM after a number of cycles before and after heat or pressure treatment. Error bars indicate one standard deviation.

retention in subsequent cycles. The schematic plots in Figures 5A and 5B compare the structure evolution for cycled LR-NCM between heat and pressure treatment. The atomic structure model based on R-$3m$ space group was constructed with zone axis [1–10] and the c lattice vector pointing upward, consistent with our TEM observations. Projected to this zone axis, the TM layer is composed of two adjacent columns of TM alternating with a column of Li due to the honeycomb superstructure. Note that the LiTM$_2$-like pattern in TM neighboring layers should stack directly on top of each other along the zone axis [1–10] in the ideal structure (Figure S1B). After electrochemical cycling, different types of defects, including Li vacancies and TM stacking fault are generated in the structure of LR-NCM material, which increases the energy of the system, creating a metastable state of the cycled material. Both heat and pressure treatment successfully provide a driving force to recover the oc-cupancy of Li in the TM layer (green arrows in Figures 5A and 5B) and the TM stacking sequence (black dashed arrows in Figures 5A and 5B). The most critical difference between the thermo and mechanical effects on the cycled structure originates

Matter
Article

CellPress
OPEN ACCESS

from the internal microstrain evolution. Microstrain is reduced to almost the same value as pristine material after heat treatment no matter how long the samples have been cycled (Figure 5D). Instead, large amount of strain residue remains in the pressure-treated sample along with surface Li/TM antisite defects.

Structural Defects and Energy State

As demonstrated in our previous work, the Li-excess particle can undergo as large as 0.6% strain during electrochemical cycling without forming intragranular cracking.[11] Substantial strain energy can be stored in Li-excess materials through dislocations generation. The dislocation density was measured to be 10^{10} cm^{-2} in Li-excess materials while the density in classical layered oxides is approximately one order of magnitude smaller. The absence of dislocations in classical layered oxides results in a strain reduction from 0.3% to 0.2% after charging to 4.5 V when intragranular cracks are directly observed using advanced electron microscopy.[37,38] The high pressure treatment in this study further confirms Li-excess layered structure after electrochemical activation can undertake 1% strain without obvious morphological destruction (Figure 4G).

The cycled material total energy after treatment can be estimated by the following expressions:

$$U_{treated} = U_{cycled} + E_{disorder} + E_{strain}$$

where the disorder energy term will increase with higher Li vacancies and TM stacking fault concentration. Both thermal and mechanical driving force are effective in reducing the material total energy through reordering the structure. Whether the treated material can be relaxed to a stable state from metastable cycled state depends on the internal strain energy. The strain energy for the supercell applied in DFT calculations can be estimated by the following equation:

$$E_{strain} = \frac{1}{2} VY\varepsilon^2$$

where V is the supercell volume, Y is the bulk modulus, and ε is the strain. The cycled material bulk modulus is determined to be ~110 GPa through the operando SXRD analysis. The strain energy for the pressure-treated sample is approximately 0.1 eV considering 1% of microstrain in the supercell as measured in the Williamson-Hall method. The strain energy increase after pressure treatment is in the same magnitude as the energy reduction by structure reordering (~0.2 eV by moving 2% Li back to the TM layer as inferred from DFT calculations). Unlike the transition from metastable to stable state through heat treatment, the cycled materials after pressure treatment transit to a different metastable state with limited total energy reduction.

Assuming the entropic and volumetric effects are small at low temperature and ambient pressure, the Gibbs free energy change for Li (de)intercalation is often approximated by the total energy difference for two Li-ion concentrations $\Delta G_r = \Delta E_r + p\Delta V_r - T\Delta S_r \approx \Delta U_r$.[39] The voltage is thus a function of free/total energy change of the overall cathode/anode reactions (Nernst equation). The difference in free/total energy between the pristine and cycled state contributes to the voltage fade observed in the electrochemical testing. Based on the mechanistic description above, the cycled material after heat treatment stays in a similar energy state as the pristine material, resulting in charging plateau and discharging average voltage recovery (Figures 5C and 5D). While the pressure effect on voltage recovery is limited and the characteristic charging plateau is not recovered even with higher cutoff voltage compared with the testing condition for heat-treated samples. The larger

CellPress
OPEN ACCESS

Matter
Article

voltage hysteresis for the sample after pressure treatment can be ascribed to the cell impedance growth resulting from surface antisite defects and spinel-type structure formation. The direct comparison between thermal and mechanical energy effect on the anionic redox-based oxide material manifests the defect chemistry is the key control factor to achieve reversible and stable anionic redox activity.

Conclusions

In summary, through combined SXRD, (S)TEM, and first principles calculations, this study pinpoints the critical influence of high pressure on the structural and electro-chemical modifications of anionic redox-based lithium-rich layered oxides. The high flexibility of the cycled structure induced by a variety of crystal defects leads to the unique response to the external stimulus: the recurring of superstructure ordering, negative bulk compressibility, and reversible lithium migration between Li and TM layer. The limiting factor for the induced formation of superlattice is the critical pressure as determined by the first principles calculations. This process does not involve any compositional change, displacive in nature, instead of long-range bulk diffusion. Despite its rarity, negative compressibility reported in this study is a highly attractive mechanical property for development of devices used in high pressure environments and producing ultrasensitive pressure detectors. Although Li (de)intercalation potential is not recovered after pressure treatment, this work suggests that crystal internal strain elimination is the key to obviate the voltage decay issue. More importantly, the unique metastability of the anionic redox-based oxide material brings opportunity to discover unusual properties, such as negative thermal expansion, negative Poisson's ratio.

EXPERIMENTAL PROCEDURES

Resource Availability

Lead Contact
Further information and requests for resources and materials should be directed to and will be fulfilled by the Lead Contact, Ying Shirley Meng (shmeng@ucsd.edu).

Materials Availability
This study did not generate new unique materials.

Date and Code Availability
This study did not generate or analyze (datasets or code).

SXRD Measurements under Operando Pressure Sweep
The cathode containing 94.5 wt % LR-NCM, 3.0 wt % conductive carbon, and 2.5 wt % polyvinylidene fluoride (PVDF) was initially cycled 18,650-typed batteries with $Li_4Ti_5O_{12}$ anode as reported previously.[13] For the initial cycle, the batteries in this study were directly charged and discharged between 3.25 and 0.5 V at 0.1 C. The fully discharged batteries after the first cycle at 0.1 C rate were dissembled in the Ar-filled glove box. The cathodes were washed with dimethyl carbonate (DMC) solvent in the glove box, and the cathode powders were obtained by scratching off the electrode from the current collector (aluminum foil) for high pressure treatment. A symmetric DAC furnished with 300 μm culet diamonds was used to conduct operando hydrostatic pressure experiments. The powder sample was placed in the 110 μm diameter holes of the T301 steel gasket. A small ruby chip was inserted into the sample compartment for pressure calibration, utilizing the R1 ruby fluorescence method.[40] Dimethylsilicone fluid was used as pressure-transmitting medium. Operando high pressure angle-dispersive SXRD experiments

Matter
Article

CellPress
OPEN ACCESS

with a wavelength of 0.62 Å and a focused beam size of ~4 × 7 μm^2 were performed at beamline 15U1, Shanghai Synchrotron Radiation Facility, China.

The structural refinement of patterns was conducted using FullProf program based on Rietveld method by assuming the space group of R-3m. The miscrostrain was analyzed by examining line broadening observed in the SXRD patterns. William-son-Hall analysis of all peaks that exhibit the best linear fitting was carried out for a quantification of microstrain changes during the pressure treatment by the following equation:

$$FW(S) \times \cos(\theta) = \frac{K \times \lambda}{Size} + 4 \times Strain \times \sin(\theta)$$

where $FW(S)$ is the calculated full-width for the sample, K is the crystallite shape factor and was set to be 0.9, the diffraction angle is given by θ, λ is the X-ray wavelength of the source. The strain was then extracted from the slope of the plot of $FW(S)\cos(\theta)$ versus $4\sin(\theta)$.

Belt-Type High Pressure Treatment

The initially cycled cathode powder was subjected to hydrostatic high pressure treatment in the range of 1–4 GPa using a Belt-type press. Samples were exposed to pressure treatment at room temperature. The pressure was slowly released after applying for either 0.5 or 1.5 h. The samples were placed in/removed from the anvil under argon atmosphere. Following the hydrostatic high pressure treatment, ex situ SXRD of the samples were taken at the Advanced Photon Source at Argonne National Laboratory on a beamline 11-BM with a wavelength of 0.41 Å. *Ex situ* SXRD patterns of the pristine and electrochemically cycled LR-NCM were also collected by the beamline 11-BM. The cycled samples were sealed in 0.8 mm Kapton capillaries to minimize air exposure. All Rietveld refinement for *ex situ* SXRD patterns was performed using the same method as described above.

Ex Situ (S)TEM/EELS/EDS/SEM Characterization

After pressure treatment in the Belt-type press, the samples were dispersed on TEM lacey carbon grid. The loading and transferring the grid to TEM were carefully controlled to prevent sample from air exposure. (HR)TEM was recorded on a field emission gun JEOL-2800 at 200 kV with Gatan OneView Camera (full 4 × 4 K resolution). STEM/EDS was performed on primary particles using the JEOL JEM-2800 at 200 kV in ADF mode. STEM-EELS was performed on JEOL JEM-ARM300CF at 300 kV, equipped with spherical aberration correctors. To minimize possible electron beam irradiation effects, EELS spectra presented in this work were acquired from areas without pre-beam irradiation. The particle sizes and morphologies were checked using ultrahigh resonance FEI Apreo SEM at an acceleration voltage of 5 kV. The particle size distribution analysis was performed on the acquired SEM images using ImageJ program.

Half Cell Electrochemical Measurements

The working electrodes were prepared by a mixture of the LR-NCM samples, conductive carbon, and PVDF binder with a weight ratio of 80: 10: 10 on an aluminum foil. To remove the residual N-methyl-2-pyrrolidone and traces of water, the electrode were dried at 80°C for 12 h under vacuum condition. Electrode discs were punched into 14 mm diameter discs from the working electrode with mass loading 3–4 mg/cm^2. Lithium metal was used as the counter electrode, Celgard 2325 as the separator, and 1 mol L^{-1} LiPF$_6$ dissolved in ethylene carbonate-DMC with the volume ratio of 3:7 as electrolyte (Gotion, USA). The cells were assembled

CellPress
OPEN ACCESS

Matter
Article

in an Ar-filled glove box (H_2O < 0.1 ppm). The galvanstatic charge/discharge test for pressure-treated samples was carried out at 0.05 C (1 C = 250 mAh g^{-1}) in the voltage range of 2.0–4.8 V. In the cyclic performance test, the cell was charged and discharged at 0.1 C. All the tests were performed at room temperature. For comparison, the electrochemical testing was also conducted on the cycled samples after heat treatment at 300°C for 1 h in the voltage range of 2.0–4.6 V.

Computation Methodology

The lithium migration pathway under high pressure treatment has been simulated with *ab initio* MD as implemented in CP2K-program. The crystal structure of $Li_{14}Ni_3Mn_7O_{24}$ was used as a starting point in the simulation. A specific $Li_{11/14}$ concentration with one oxygen vacancy was chosen to simulate the discharged state obtained experimentally. The full range of different configurations for the unit cell of $Li_{11}Ni_3Mn_7O_{23}$ were tested in our previous work and the model with the lowest energy was used in this work.[13] And then a supercell model composed of two-formula units of $Li_{11}Ni_3Mn_7O_{23}$ was built and called as the 112 supercell (1 × 1 × 2 with respect to the unit cell axis *a*, *b*, and *c*). The supercells were optimized before starting the actual MD simulations.

Calculations were performed with the PBE density functional using the molecular optimized short-range DZVP (DZVPMOLOPT-SR) basis set combined with the GTH pseudopotentials.[41,42] Molecular optimized (MOLOPT) basis sets have generally been found to perform better than similarly sized or slightly larger basis sets. Grimme's DFT-D3 dispersion corrections were incorporated in the computations.[43] The CSVR thermostat was used with the time step of 100.0 fs. The NVT ensemble was selected for the MD runs. Cutoff for planewaves was 600 Ry. Simulations were performed as cell optimization with 50 MD steps per cell optimization cycle with the time step of 0.5 fs. VMD, OVITO, and VESTA programs were used for the visualization of simulation data.

The NEB method was used to find the minimum energy path and the energy barrier for lithium migration inside the 112 supercell. Calculations were performed in the spin polarized GGA + U approximations to the DFT as implemented in the Vienna *ab initio* simulation package.[44,45] The same effective U value as applied in our previous report was used to enforce the effect of localized d electrons of the TM ions.[46] We used the PBE exchange correlation, and a plane-wave representation for the wave function with a cutoff energy of 520 eV.[47] The Brillouin zone was sampled with a dense k-points mesh by Gamma packing. To obtain the energy barrier for lithium migration path, the atomic positions and cell parameters were fully relaxed.

SUPPLEMENTAL INFORMATION

Supplemental Information can be found online at https://doi.org/10.1016/j.matt.2020.10.026.

Matter
Article

thank beamline 15U1 (Shanghai Synchrotron Radiation Facility) for providing the beam time and assistance for operando pressure sweep. High pressure treatments in the Belt-type press were performed at Laboratorio Complutense de Altas Presiones (UCM, Madrid). J.M.G.-A. and M.E.A.-d.D. thank MINECO and Agencia Estatal de Investigación (AEI)/Fondo Europeo de Desarrollo Regional (FEDER/UE) for funding the Project PID2019-106662RB-C44, and support from the MALTA-Consolider Network (RED2018-102612-T). *Ex situ* SXRD was collected at beamline 11-BM of the Advanced Photon Source at Argonne National Laboratory supported by the U.S. Department of Energy, Office of Science, Office of Basic Energy Sciences, under contract no. DE-AC02-06CH11357. This work used the Extreme Science and Engineering Discovery Environment (XSEDE), which is supported by National Science Foundation grant no. ACI-1548562. (S)TEM/EDS and EELS were performed at the UC Irvine Materials Research Institute (IMRI) using instrumentation funded in part by the National Science Foundation Major Research Instrumentation Program under grant no. CHE-1338173. SEM was performed in part at the San Diego Nanotechnology Infrastructure (SDNI), a member of the National Nanotechnology Coordinated Infrastructure, which is supported by the National Science Foundation (grant no. ECCS-1542148). M.Z. thanks Dr. Enyue Zhao for his assistance with structural refinement for comparing the R-3m and C2/m space group.

AUTHOR CONTRIBUTIONS

M.Z., B.Q., and Y.S.M. designed the experiments. M.Z. and Y.S.M. performed the mechanism analysis. B.Q., C.Y., and S.J. conducted the synchrotron X-ray diffraction measurements under operando pressure sweep. H.L. and M.Z. performed operando SXRD data analysis. J.M.G.-A. and M.E.A.-d.D. performed Belt-type pressure treatment. M.O. and M.Z. performed the first principles calculations. M.Z. collected and analyzed *ex situ* SXRD data, (S)TEM imaging, EDS, and EELS spectra. B.Q., Y.L., and W.Y. conducted electrochemical testing and SEM characterization. Y.S.M. and Z.L. supervised the research. M.Z. and B.Q. co-wrote the manuscript. All authors contributed to the discussion and provided feedback on the manuscript.

DECLARATION OF INTERESTS

The authors declare no competing interests.

REFERENCES

1. Radin, M.D., Hy, S., Sina, M., Fang, C., Liu, H., Vinckeviciute, J., Zhang, M., Whittingham, M.S., Meng, Y.S., and Van der Ven, A. (2017). Narrowing the gap between theoretical and practical capacities in Li-ion layered oxide cathode materials. Adv. Energy Mater. 7, 1602888.

2. Johnson, C.S., Kim, J.-S., Lefief, C., Li, N., Vaughey, J.T., and Thackeray, M.M. (2004). The significance of the Li_2MnO_3 component in "composite" $xLi_2MnO_3 \cdot (1 - x)LiMn_{0.5}Ni_{0.5}O_2$ electrodes. Electrochem. Commun. 6, 1085–1091.

3. Lu, Z., MacNeil, D.D., and Dahn, J.R. (2001). Layered cathode materials $Li[Ni_xLi_{(1/3-2x/3)}Mn_{(2/3-x/3)}]O_2$ for lithium-ion batteries. Electrochem. Solid-state Lett. 4, A191.

4. Seo, D.-H., Lee, J., Urban, A., Malik, R., Kang, S., and Ceder, G. (2016). The structural and chemical origin of the oxygen redox activity in layered and cation-disordered Li-excess cathode materials. Nat. Chem. 8, 692–697.

5. Luo, K., Roberts, M.R., Hao, R., Guerrini, N., Pickup, D.M., Liu, Y.-S., Edström, K., Guo, J., Chadwick, A.V., Duda, L.C., et al. (2016). Charge-compensation in 3D-transition-metal-oxide intercalation cathodes through the generation of localized electron holes on oxygen. Nat. Chem. 8, 684–691.

6. Ben Yahia, M., Vergnet, J., Saubanère, M., and Doublet, M.L. (2019). Unified picture of anionic redox in Li/Na-ion batteries. Nat. Mater. 18, 496–502.

7. Zhao, E., Zhang, M., Wang, X., Hu, E., Liu, J., Yu, X., Olguin, M., Wynn, T.A., Meng, Y.S., Page, K., et al. (2020). Local structure adaptability through multi cations for oxygen redox accommodation in Li-rich layered oxides. Energy Storage Mater 24, 384–393.

8. Okubo, M., and Yamada, A. (2017). Molecular orbital principles of oxygen-redox battery electrodes. ACS Appl. Mater. Inter. 9, 36463–36472.

9. Qiu, B., Zhang, M., Xia, Y., Liu, Z., and Meng, Y.S. (2017). Understanding and controlling anionic electrochemical activity in high-capacity oxides for next generation Li-ion batteries. Chem. Mater. 29, 908–915.

10. Gent, W.E., Lim, K., Liang, Y., Li, Q., Barnes, T., Ahn, S.-J., Stone, K.H., McIntire, M., Hong, J., Song, J.H., et al. (2017). Coupling between oxygen redox and cation migration explains unusual electrochemistry in lithium-rich layered oxides. Nat. Commun. 8, 2091.

11. Singer, A., Zhang, M., Hy, S., Cela, D., Fang, C., Wynn, T.A., Qiu, B., Xia, Y., Liu, Z., Ulvestad, A., et al. (2018). Nucleation of dislocations and their dynamics in layered oxide cathode materials during battery charging. Nat. Energy 3, 641–647.

12. Hu, E., Yu, X., Lin, R., Bi, X., Lu, J., Bak, S., Nam, K.W., Xin, H.L., Jaye, C., Fischer, D.A., et al. (2018). Evolution of redox couples in Li- and Mn-rich cathode materials and mitigation of voltage fade by reducing oxygen release. Nat. Energy 3, 690–698.

13. Qiu, B., Zhang, M., Lee, S.-Y., Liu, H., Wynn, T.A., Wu, L., Zhu, Y., Wen, W., Brown, C.M., Zhou, D., et al. (2020). Metastability and reversibility of anionic redox-based cathode for high-energy rechargeable batteries. Cell Rep. Phys. Sci. 1, 100028.

14. Assat, G., Glazier, S.L., Delacourt, C., and Tarascon, J.M. (2019). Probing the thermal effects of voltage hysteresis in anionic redox-based lithium-rich cathodes using isothermal calorimetry. Nat. Energy 4, 647–656.

15. Goodwin, A.L., Keen, D.A., and Tucker, M.G. (2008). Large negative linear compressibility of Ag$_3$[Co(CN)$_6$]. Proc. Natl. Acad. Sci. U S A 105, 18708–18713.

16. Arroyo y de Dompablo, M.E., Amador, U., Gallardo-Amores, J.M., Morán, E., Ehrenberg, H., Dupont, L., and Dominko, R. (2009). Polymorphs of Li$_3$PO$_4$ and Li$_2$MSiO$_4$ (M = Mn, Co). The role of pressure. J. Power Sources 189, 638–642.

17. Arroyo-De Dompablo, M.E., Gallardo-Amores, J.M., and Amador, U. (2005). Lithium insertion in the high-pressure polymorph of FePO$_4$ computational predictions and experimental findings. Electrochem. Solid State Lett. 8, A564.

18. García-Moreno, O., Alvarez-Vega, M., García-Alvarado, F., García-Jaca, J., Gallardo-Amores, J.M., Sanjuán, M.L., and Amador, U. (2001). Influence of the structure on the electrochemical performance of lithium transition metal phosphates as cathodic materials in rechargeable lithium batteries: a new high-pressure form of LiMPO$_4$ (M = Fe and Ni). Chem. Mater. 13, 1570–1576.

19. Amador, U., Gallardo-Amores, J.M., Heymann, G., Huppertz, H., Morán, E., and Arroyo y de Dompablo, M.E. (2009). High pressure polymorphs of LiCoPO$_4$ and LiCoAsO$_4$. Solid State Sci. 11, 343–348.

20. Zhang, Y., Wang, L., Yang, J., He, X., Wang, J., Zhang, Y., Jin, Y., Li, Y., and Xiong, L. (2015). Effect of pressure on the structural properties of Li[Li$_{0.1}$Ni$_{0.35}$Mn$_{0.55}$]O$_2$. AIP Adv. 5, 047106.

21. Fell, C.R., Lee, D.H., Meng, Y.S., Gallardo-Amores, J.M., Morán, E., and Arroyo-De Dompablo, M.E. (2012). High pressure driven structural and electrochemical modifications in layered lithium transition metal intercalation oxides. Energy Environ. Sci. 5, 6214–6224.

22. Zhang, M., Liu, H., Liu, Z., Fang, C., and Meng, Y.S. (2018). Modified coprecipitation synthesis of mesostructure-controlled Li-rich layered oxides for minimizing voltage degradation. ACS Appl. Energy Mater. 1, 3369–3376.

23. Liu, H., Chen, Y., Hy, S., An, K., Venkatachalam, S., Qian, D., Zhang, M., and Meng, Y.S. (2016). Operando lithium dynamics in the Li-rich layered oxide cathode material via neutron diffraction. Adv. Energy Mater. 6, 1502143.

24. Birch, F. (1947). Finite elastic strain of cubic crystals. Phys. Rev. 71, 809–824.

25. Lee, E., and Persson, K.A. (2014). Structural and chemical evolution of the layered Li-excess Li$_x$MnO$_3$ as a function of Li content from first-principles calculations. Adv. Energy Mater. 4, 1400498.

26. Qian, D., Xu, B., Chi, M., and Meng, Y.S. (2014). Uncovering the roles of oxygen vacancies in cation migration in lithium excess layered oxides. In Physical Chemistry Chemical Physics (Royal Society of Chemistry), pp. 14665–14668.

27. Yu, H., So, Y.G., Kuwabara, A., Tochigi, E., Shibata, N., Kudo, T., Zhou, H., and Ikuhara, Y. (2016). Crystalline grain interior configuration affects lithium migration kinetics in Li-rich layered oxide. Nano Lett. 16, 2907–2915.

28. Li, Q., Yao, Z., Lee, E., Xu, Y., Thackeray, M.M., Wolverton, C., Dravid, V.P., and Wu, J. (2019). Dynamic imaging of crystalline defects in lithium-manganese oxide electrodes during electrochemical activation to high voltage. Nat. Commun. 10, 1–7.

29. Jarvis, K.A., Deng, Z., Allard, L.F., Manthiram, A., and Ferreira, P.J. (2011). Atomic structure of a lithium-rich layered oxide material for lithium-ion batteries: evidence of a solid solution. Chem. Mater. 23, 3614–3621.

30. Ahmed, S., Bianchini, M., Pokle, A., Munde, M.S., Hartmann, P., Brezesinski, T., Beyer, A., Janek, J., and Volz, K. (2020). Visualization of light elements using 4D STEM: the layered-to-rock salt phase transition in LiNiO$_2$ cathode material. Adv. Energy Mater. 10, 2001026.

31. Soriano, L., Abbate, M., Vogel, J., Fuggle, J.C., Fernández, A., González-Elipe, A.R., Sacchi, M., and Sanz, J.M. (1993). The electronic structure of mesoscopic NiO particles. Chem. Phys. Lett. 208, 460–464.

32. Carroll, K.J., Qian, D., Fell, C., Calvin, S., Veith, G.M., Chi, M., Baggetto, L., and Meng, Y.S. (2013). Probing the electrode/electrolyte interface in the lithium excess layered oxide Li$_{1.2}$Ni$_{0.2}$Mn$_{0.6}$O$_2$. Phys. Chem. Chem. Phys. 15, 11128–11138.

33. Kurata, H., and Colliex, C. (1993). Electron-energy-loss core-edge structures in manganese oxides. Phys. Rev. B 48, 2102–2108.

34. Yang, W., Huang, X., Harder, R., Clark, J.N., Robinson, I.K., and Mao, H.K. (2013). Coherent diffraction imaging of nanoscale strain evolution in a single crystal under high pressure. Nat. Commun. 4, 1–6.

35. Williamson, G.K., and Hall, W.H. (1953). X-ray line broadening from filed aluminium and wolfram. Acta Metall. 1, 22–31.

36. Assat, G., and Tarascon, J.M. (2018). Fundamental understanding and practical challenges of anionic redox activity in Li-ion batteries. Nat. Energy 3, 373–386.

37. Wang, H. (1999). TEM study of electrochemical cycling-induced damage and disorder in LiCoO$_2$ cathodes for rechargeable lithium batteries. J. Electrochem. Soc. 146, 473.

38. Yan, P., Zheng, J., Gu, M., Xiao, J., Zhang, J.G., and Wang, C.M. (2017). Intragranular cracking as a critical barrier for high-voltage usage of layer-structured cathode for lithium-ion batteries. Nat. Commun. 8, 1–9.

39. Aydinol, M., Kohan, A., Ceder, G., Cho, K., and Joannopoulos, J. (1997). Ab initio study of lithium intercalation in metal oxides and metal dichalcogenides. Phys. Rev. B Condens. Matter Mater. Phys. 56, 1354–1365.

40. Mao, H.K., Xu, J., and Bell, P.M. (1986). Calibration of the ruby pressure gauge to 800 kbar under quasi-hydrostatic conditions. J. Geophys. Res. 91, 4673.

41. VandeVondele, J., and Hutter, J. (2007). Gaussian basis sets for accurate calculations on molecular systems in gas and condensed phases. J. Chem. Phys. 127, 114105.

42. Goedecker, S., and Teter, M. (1996). Separable dual-space Gaussian pseudopotentials. Phys. Rev. B Condens. Matter Mater. Phys. 54, 1703–1710.

43. Grimme, S., Antony, J., Ehrlich, S., and Krieg, H. (2010). A consistent and accurate ab initio parametrization of density functional dispersion correction (DFT-D) for the 94 elements H-Pu. J. Chem. Phys. 132, 154104.

44. Kresse, G., and Furthmüller, J. (1996). Efficiency of ab-initio total energy calculations for metals and semiconductors using a plane-wave basis set. Comput. Mater. Sci. 6, 15–50.

45. Joubert, D. (1999). From ultrasoft pseudopotentials to the projector augmented-wave method. Phys. Rev. B Condens. Matter Mater. Phys. 59, 1758–1775.

46. Wynn, T.A., Fang, C., Zhang, M., Liu, H., Davies, D.M., Wang, X., Lau, D., Lee, J.Z., Huang, B.-Y., Fung, K.-Z., et al. (2018). Mitigating oxygen release in anionic-redox-active cathode materials by cationic substitution through rational design. J. Mater. Chem. A 6, 24651–24659.

47. Perdew, J.P., Burke, K., and Ernzerhof, M. (1996). Generalized gradient approximation made simple. Phys. Rev. Lett. 77, 3865–3868.